Energy Storage Materials 76 (2025) 104169

Contents lists available at ScienceDirect

Energy Storage Materials

journal homepage: www.elsevier.com/locate/ensm

Surface stabilization for enhancing air/moisture resistance of layered Ni-rich oxide cathodes

Zhouliang Tan [a], Feng Xu [a], Ruizhuo Zhang [b], Yudai Huang [a,*], Xia Liu [a], Shupeng Yang [d,e], Yizhong Guo [d,e], Qingcui Liu [a], Tianlong Wu [a], Yingde Huang [c,*], Torsten Brezesinski [b], Yu Tang [d,e,*], Wengao Zhao [b,d,e,*]

[a] State Key Laboratory of Chemistry and Utilization of Carbon Based Energy Resources, College of Chemistry, Xinjiang University, Urumqi 830017, China
[b] Institute of Nanotechnology, Karlsruhe Institute of Technology (KIT), Karlsruhe 76131, Germany
[c] School of Materials Science and Engineering, Zhengzhou University, Zhengzhou 450001, China
[d] Key Laboratory of Nonferrous Metal Chemistry and Resources Utilization of Gansu Province, College of Chemistry and Chemical Engineering, Lanzhou University, Lanzhou 730000, China
[e] State Key Laboratory of Baiyunobo Rare Earth Resource Researches and Comprehensive Utilization, Baotou Research Institute of Rare Earths, Baotou 014030, China

ARTICLE INFO

Keywords:
Ni-rich cathode
Coating
Chemical grafting
Ambient air resistance
Residual lithium

ABSTRACT

Layered Ni-rich oxides ($LiNi_xCo_yMn_zO_2$, with $x \geq 0.8$ and $x + y + z = 1$) are promising cathode materials for high-energy-density lithium-ion batteries (LIBs) owing to their high specific capacity and high operating voltage. However, the Ni-rich cathode suffers from notorious deterioration when in contact with ambient air, primarily driven by nickel's multivalent ($Ni^{2+}/Ni^{3+}/Ni^{4+}$) reactions and humidity sensitivity. In this study, we report a novel surface modification strategy for $LiNi_{0.83}Co_{0.12}Mn_{0.05}O_2$ (NCM83) via Li_xSiO_y coating, achieved through chemical grafting using the silane coupling agent, (3-aminopropyl) triethoxysilane (KH550), followed by thermal treatment. The modified NCM83 exhibits enhanced moisture resistance due to a superhydrophobic surface that suppresses detrimental reactions between residual lithium species (Li_2O, LiOH, etc.) and water. Furthermore, the Li_xSiO_y coating mitigates mechanical degradation by facilitating strain relaxation. Notably, the modified NCM83 retains high electrochemical performance after 28 days of air exposure, delivering a specific capacity of 157 mAh g^{-1} after 100 cycles at 1C, compared to 108 mAh g^{-1} for the uncoated counterpart. Overall, these findings present an effective strategy for improving upon the surface stability of Ni-rich cathodes, facilitating their processing and paving the way for large-scale applications in high-energy LIBs.

1. Introduction

The rapid development of electric vehicles (EVs) has intensified the demand for high-performance, rechargeable lithium-ion batteries (LIBs) [1]. To meet the endurance requirements of EVs, LIBs must achieve significantly higher energy densities, primarily dictated by the cathode's specific capacity and operating voltage [2,3]. Compared with $LiCoO_2$ [4], $LiFePO_4$ [5], and $LiMn_2O_4$ cathode materials [6], layered Ni-rich oxides ($LiNi_xCo_yMn_{1-x-y}O_2$, with $x \geq 0.8$; referred to as NCM or NMC) have emerged as viable candidates for next-generation LIBs, offering high reversible specific capacities ($q_{dis} > 200$ mAh g^{-1}) and good rate capabilities [7–9]. Despite these advantages, Ni-rich cathodes encounter significant challenges in practical applications, particularly instabilities in ambient atmosphere, stemming from the unique electronic structure of nickel ions ($Ni^{2+/3+/4+}$) and sensitivity to moist air [10].

Under ambient atmospheric conditions, Ni-rich cathode particles readily adsorb H_2O and CO_2, forming LiOH and Li_2CO_3 residues on the surface [11]. These inactive lithium compounds increase the pH of the electrode slurry, resulting in a gel-like state during preparation and hindering uniform coating on the current collector [12]. Additionally, airborne components react with active oxygen species generated by the reduction of Ni^{3+} on the surface, leading to the formation of impurities that can induce detrimental subsurface phase transformations, converting the layered structure into a redox-inactive NiO-like rock-salt structure [13]. More seriously, such transformations negatively impact rate performance and cycling stability by obstructing lithium diffusion channels and increasing the energy barrier for (de)lithiation [14].

* Corresponding authors.
E-mail addresses: huangyd@xju.edu.cn (Y. Huang), ydhuang@zzu.edu.cn (Y. Huang), tangyu@lzu.edu.cn (Y. Tang), wengao.zhao@kit.edu (W. Zhao).

https://doi.org/10.1016/j.ensm.2025.104169
Received 12 January 2025; Received in revised form 24 February 2025; Accepted 8 March 2025
Available online 9 March 2025

Furthermore, the anisotropic volume expansion and contraction of the unit cell during battery operation generate microcracks (mainly intergranular cracks) inside the particles, which then propagate to surface [15], further accelerating capacity decay. Intergranular cracks facilitate electrolyte penetration along the newly generated "channels" within the particles, resulting in the accumulation of the detrimental NiO-like rock-salt phase from the reduction of active Ni^{4+} at high states of charge [16]. Therefore, strategies to mitigate both surface and bulk structural instabilities are crucial for the practical application of Ni-rich cathodes in advanced LIBs.

Effective modification strategies, such as washing, secondary sintering, and surface coating, have been proposed to decrease the air sensitivity of Ni-rich cathode materials [17]. Water washing removes excess lithium, including LiOH and Li_2CO_3, thereby helping to lower the electrode slurry's pH and prevent gelling during fabrication [18]. However, it may negatively affect the subsurface structure (Li^+/H^+ exchange), increasing instabilities during charging/discharging [19] and rendering the material more susceptible to air exposure, thus necessitating further protective measures [20]. Secondary sintering effectively eliminates surface lithium species through thermal decomposition and solid-state reactions without wastewater production, making it environmentally friendly [21]. However, it cannot prevent surface degradation upon prolonged air exposure and requires precise control of parameters [22], increasing manufacturing complexity. In contrast, surface coating is the most effective strategy for enhancing the interfacial stability of Ni-rich cathodes [23]. Protective coatings isolate the cathode from ambient air, reducing interactions with moisture and CO_2, thereby preventing formation of lithium residues on the particle surface [24,25]. They also serve as a barrier against electrolyte penetration and mitigate crack propagation by providing mechanical support, ultimately enhancing structural integrity [26]. Notably, selecting compatible coating materials is essential to avoid performance degradation.

In this study, we utilized chemical grafting with the hydrophobic silane coupling agent (KH550) to modify the surface of $LiNi_{0.83}Co_{0.12}Mn_{0.05}O_2$ (NCM83), aiming at increasing chemical and environmental stability. Through structural characterizations and theoretical calculations, we provide insights into the origin of air instability and its effects on electrochemical activity. Our experimental results demonstrate that the Li_xSiO_y coating is capable of inhibiting adverse chemical reactions with H_2O and CO_2, effectively addressing the air sensitivity of the Ni-rich cathode. Additionally, the coating improves the tolerance of NCM83 to strain at high states of charge by reducing *c*-lattice parameter shrinkage. Consequently, the surface-coated cathode material exhibits superior cycling performance and faster charge-transfer kinetics compared to pristine NCM83 (showing reduced initial specific discharge capacity after 28 days of air exposure). Taken together, this work presents an industrial solution for the large-scale application of Ni-rich cathodes, stabilizing their surface structure and enhancing chemical stability against ambient air/moisture.

2. Experimental

2.1. Material preparation

The $LiNi_{0.83}Co_{0.12}Mn_{0.05}O_2$ (NCM83) cathode material was synthesized by a facile solid-state method. A $Ni_{0.83}Co_{0.12}Mn_{0.05}(OH)_2$ precursor was mixed with $LiOH{\cdot}H_2O$ in a molar ratio 1:1.05, then calcined at 500 °C for 4 h, and finally at 780 °C for 12 h. A uniform Li_xSiO_y coating was applied to the surface of the NCM83 particles through a wet-dipping method. The silane coupling agent (KH550, 98 wt.%, Shanghai YuanYe Biotechnology Co., Ltd.) was dissolved in a mixture of absolute alcohol and water (2:1volume ratio) to hydrolyze at 60 °C. NCM83 powder was dispersed into this solution and stirred at 80 °C for 6 h. After solid-liquid separation, the material was dried at 100 °C for 12 h, followed by calcination at 600 °C for 6 h. The resultant samples are referred to as NCM83@Si-5, NCM83@Si-10, and NCM83@Si-15, depending on the mass fraction of KH550 (0.5, 1.0, and 1.5 wt.%, respectively). For comparison, a control sample (NCM83@Si-0) was prepared without using any KH550.

2.2. Air exposure

The samples were placed in a controlled environment at 25 °C and 50 % relative humidity for either 14 or 28 days. The respective samples after air exposure are referred to as 14NCM83@Si-0, 14NCM83@Si-5, 14NCM83@Si-10, and 14NCM83@Si-15 or 28NCM83@Si-0, 28NCM83@Si-5, 28NCM83@Si-10, and 28NCM83@Si-15, respectively.

2.3. Characterization

X-ray diffraction (XRD, Empyrean 2) analysis was performed to examine the crystal structure with a scanning angle of 10−80°. Rietveld refinements were performed using the GSAS software. The surface morphology was probed using field-emission scanning electron microscopy (SEM, JSM-7900F, JEOL) and high-resolution transmission electron microscopy (HRTEM, Talos F200X). The surface elemental composition was determined by X-ray photoelectron spectroscopy (XPS, Kratos), with depth analysis performed via argon ion etching. The Ni l-edge and O k-edge were measured using synchrotron radiation at the NSRL (Soochow beamlines MCD-A and MCD-B). The residual lithium content was quantified by neutralization titration using 0.1 M HCl as titrant, with an endpoint pH of 7.0.

2.4. Electrochemical testing

Cathodes were prepared by mixing the active material, polyvinylidene fluoride (PVDF), and acetylene black in an 8:1:1 mass ratio, followed by the addition of 1-methyl-2-pyrrolidone (NMP) as solvent to form a slurry. The slurry was coated onto aluminum foil and dried at 90 °C for 8 h. Electrodes were punched into 13 mm disks (having areal loadings of active material of 2−3 mg cm^{-2}) and used to assemble 2032-type coin cells with a lithium-metal anode, a polypropylene separator (Celgard 2400), and 1 M $LiPF_6$ dissolved in EC, DEC, and EMC (1:1:1 by weight) as electrolyte. Charge-discharge tests were mostly conducted between 2.8 and 4.3 V vs. Li^+/Li using a Neware battery test system (Shenzhen Neware Technology Co., Ltd.). Electrochemical impedance spectroscopy (EIS) and cyclic voltammetry (CV) measurements were performed using an electrochemical workstation (VMP-300, Bio-Logic).

2.5. Density functional theory (DFT) calculations

First-principles calculations were performed using DFT, with detailed methodologies provided in the Supporting Information.

3. Results and discussion

3.1. Structural characterization

As illustrated in Fig. 1**a**, a hydrophobic Li_xSiO_y coating was introduced onto the surface of NCM83 particles via a grafting reaction, aiming to enhance air stability. Initially, hydrolyzed KH550 adsorbed on the free surface, forming Si−O−Li bonds with surface oxygen atoms. Upon thermal treatment, the hydrolyzed KH550 decomposed, resulting in the formation of a uniform Li_xSiO_y coating. Inductively coupled plasma (ICP)-assisted elemental analysis confirmed that the Si content largely agrees with the targeted KH550 concentration (see **Table S1**). X-ray diffraction (XRD) indicated that the diffraction peaks detected for all samples (see **Figure S1**) match the expected hexagonal α-$NaFeO_2$ structure ($R-3m$ space group). The apparent splitting of the (006)/(012) and (018)/(110) reflections demonstrates that the surface modification does not alter the bulk structure of NCM83 [27]. No crystalline impurities were observed, which can likely be attributed to the low

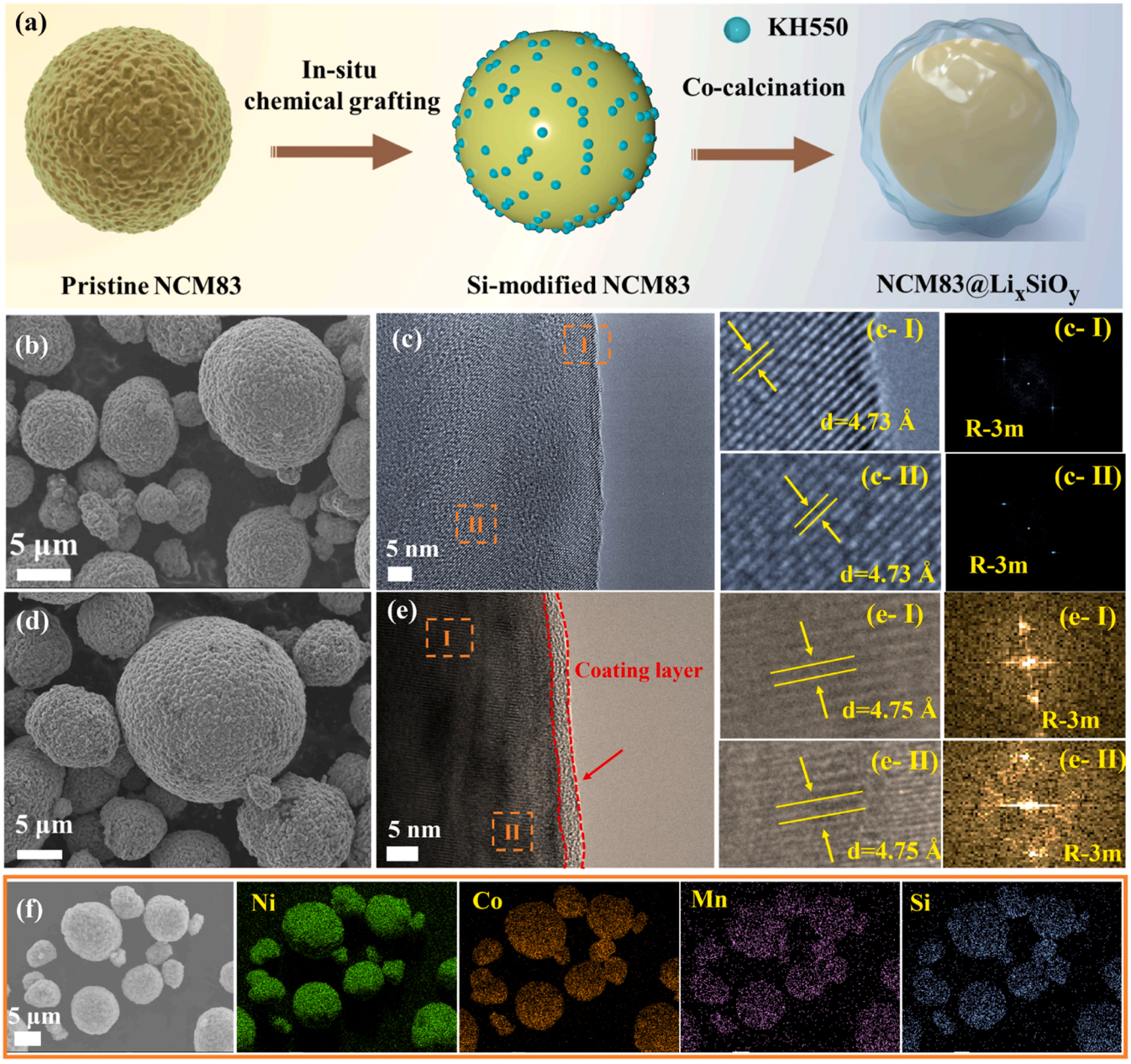

Fig. 1. (a) Schematic illustration of the chemical grafting process of KH550 onto the NCM83 surface. SEM images of (b) NCM83@Si-0 and (d) NCM83@Si-10. TEM images at different magnifications of (c) NCM83@Si-0 and (e) NCM83@Si-10 and corresponding FFT patterns. (f) EDS mapping of NCM83@Si-10.

concentration and amorphous nature of the Li_xSiO_y coating.

Scanning electron microscopy (SEM) imaging of NCM83@Si-0 and NCM83@Si-10 (see Fig. 1**b** and **d**) revealed spherical secondary particle morphologies. As can be seen, the latter particles were composed of primary grains of size 200–300 nm. NCM83@Si-10 exhibited smoother, more round-shaped particles, with the primary grains largely masked by the coating. High-resolution transmission electron microscopy (HRTEM) imaging revealed clear lattice fringes (4.73 Å), corresponding to the (003) planes of the layered structure of NCM83@Si-0 (see Fig. 1**c**). In contrast, NCM83@Si-10 exhibited an amorphous ~4 nm thick surface coating without disrupting the underlying crystal structure (see Fig. 1**e**). Increasing the KH550 content to 5 % resulted in the appearance of additional XRD reflections, matching well with Li_2SiO_3 (see **Figure S2**), thus confirming the formation of a lithium silicate coating, which facilitates lithium transport and acts as a protective barrier against interactions with air and electrolyte. Besides, Si 2p X-ray photoelectron spectroscopy (XPS) depth profile analysis was performed to gain more insight into the elemental composition of NCM83@Si-10. As shown in **Figure S3**, Si is only detected near the surface. This result confirms that it is enriched on the surface rather than diffusing into the bulk during the heat-treatment process. Infrared (IR) spectra (see **Figure S4**) further support the presence of lithium silicate through the presence of additional bands, complementing the original OH^-/H_2O and CO_3^{2-} vibrations observed for NCM83@Si-0 and NCM83@Si-10 [28]. Additionally, EDS mapping of NCM83@Si-10 (see Fig. 1**f**) confirmed the uniform distribution of Si on the particle surface, demonstrating successful encapsulation by the hydrophobic Li_xSiO_y coating.

3.2. *Structural evolution upon air exposure*

To investigate the effects of ambient air exposure on morphology and microstructure of the NCM83 cathode, both coated and uncoated

samples were treated under controlled conditions [temperature = (25 ± 1) °C, relative humidity = 50 %]. SEM images of NCM83@Si-0 and NCM83@Si-10 taken before and after 14 and 28 days of exposure are presented in Fig. 2**a**–**f**. After 14 days, NCM83@Si-0 displayed small flakes on its surface, leading to blurred (primary) grain boundaries (see Fig. 2**b**). By 28 days, a thick layer of impurities formed (see Fig. 2**c**), attributed to reactions with atmospheric moisture. The latter led to lithium migration from the bulk phase and H^+ penetration, thereby forming LiOH and Li_2CO_3 impurities. In contrast, the NCM83@Si-10 maintained a clean surface, with the primary particles remaining well-defined even after 28 days of air exposure (see Fig. 2**e** and **f**). These findings suggest that the Li_xSiO_y coating effectively prevents ion-exchange reactions at the electrode|air interface, thereby enhancing stability.

XPS analysis confirmed an increase in carbonate content in NCM83@Si-0, from 10.3 % for the pristine sample to 42.2 % after 28 days, while NCM83@Si-10 exhibited minor changes, from 9.7 % to 14.7 % (see Fig. 2**g** and **h**). These results underscore the effectiveness of the protective coating in preventing reactions of NCM83 with H_2O and CO_2 in the air, accounting for the enhanced cycling stability of NCM83@Si-10. The residual lithium species present on the cathode surface were quantified by chemical titration measurements (see Fig. 2**i**). In general, NCM83@Si-0 demonstrated significantly higher residual lithium levels compared to NCM83@Si-10, indicating much higher sensitivity toward air. After 14 and 28 days, the residual lithium content in NCM83@Si-0 strongly increased to 1425 and 1872 ppm, respectively, due to continuous Li^+/H^+ exchange, while that in NCM83@Si-10 remained fairly constant. These results provide profound evidence that the Li_xSiO_y coating enhances air stability by limiting the formation of surface impurities.

To examine the properties of coating, dynamic contact angle measurements were conducted on both NCM83@Si-0 and NCM83@Si-10 after varying periods of air exposure. Pristine NCM83@Si-0 exhibited a relatively low contact angle of 23.4° (see Fig. 3**a**), indicative of a hydrophilic surface. In contrast, pristine NCM83@Si-10 revealed a much higher contact angle of 53.1° (see Fig. 3**d**), signifying increased water repellency. NCM83@Si-0 became even more hydrophilic upon air exposure, with the contact angle decreasing to 19.6° and 16.7° after 14 and 28 days, respectively (see Fig. 3**b** and **c**), likely due to formation of LiOH and Li_2CO_3 on the top surface. Conversely, NCM83@Si-10 maintained its hydrophobic nature, with only slight decreases in contact angle to 52° after 14 days and to 50° after 28 days (see Fig. 3**e** and **f**).

XRD analysis also confirmed that both materials retained their α-$NaFeO_2$-type structure after air exposure (see Fig. 3**g** and **h**). However, NCM83@Si-0 exhibited a (003) peak shift by 0.76° to larger angles after 28 days, indicating increased layer spacing [23]. In contrast, NCM83@Si-10 only showed a shift by 0.21°, suggesting effective bulk passivation. Rietveld refinements further validated these findings. As shown in **Figures S5**–**S7** and **Tables S2**–**S4**, the relatively low discrepancy (error index) values indicate good reliability. After 28 days,

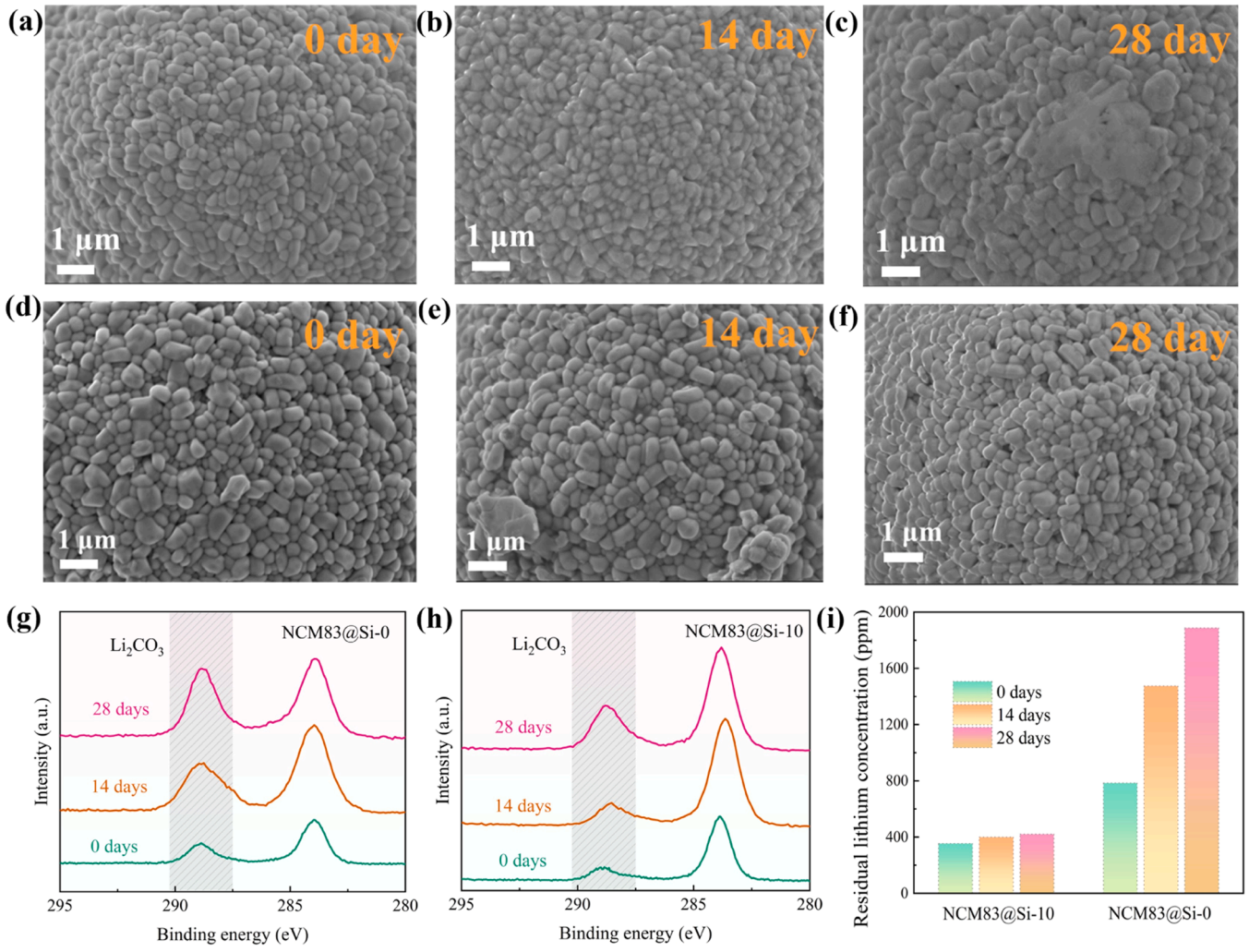

Fig. 2. SEM images of (a–c) NCM83@Si-0 and (d–f) NCM83@Si-10 taken before and after air exposure for 14 and 28 days and (g, h) corresponding normalized C 1 s XP spectra. (i) Comparison of residual lithium concentrations before and after air exposure.

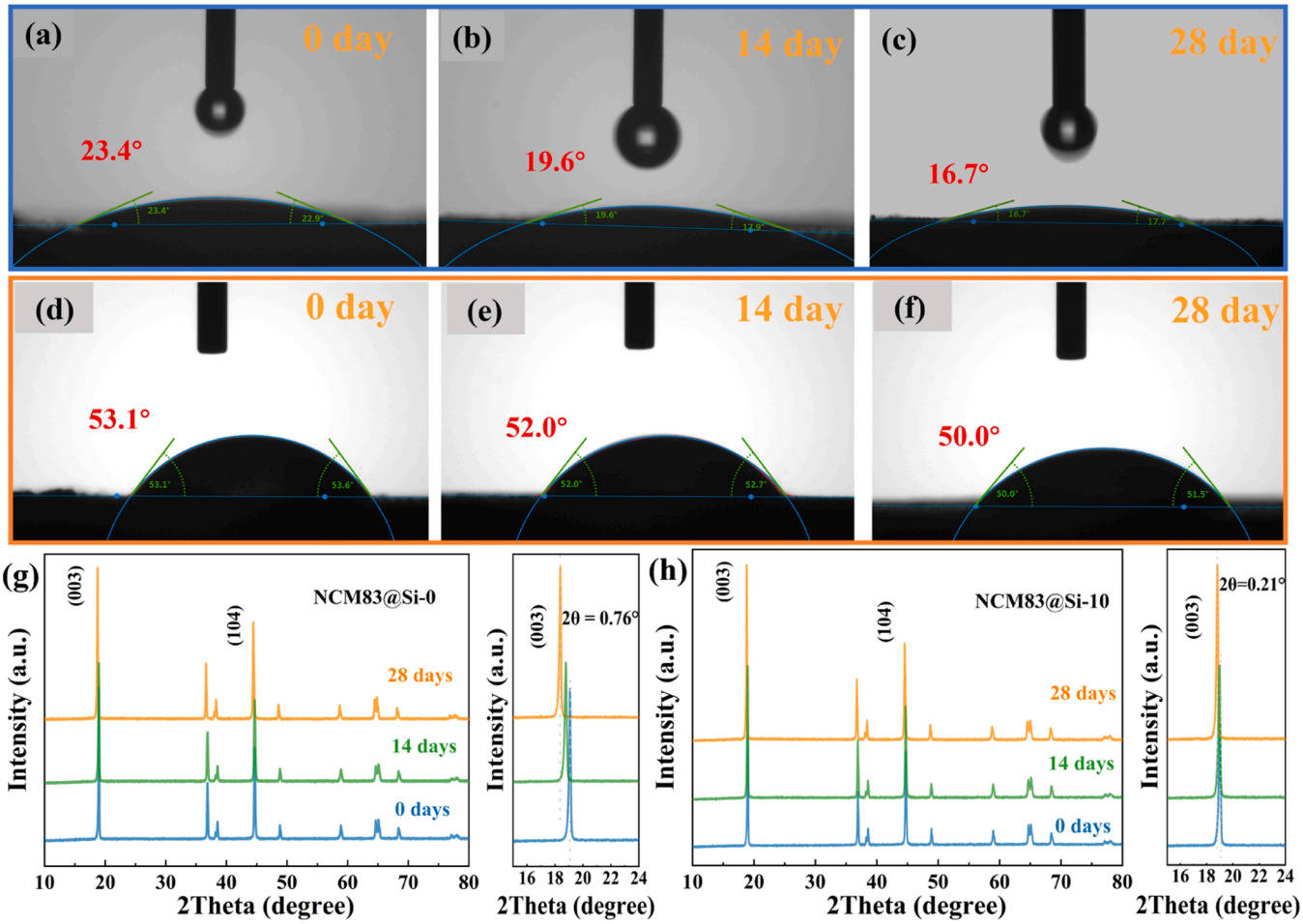

Fig. 3. Contact angles of water on (a–c) NCM83@Si-0 and (d–f) NCM83@Si-10 before and after air exposure for 14 and 28 days and (g, h) corresponding XRD patterns.

the *c* lattice parameter of NCM83@Si-0 increased from 14.163 to 14.170 Å, while that of NCM83@Si-10 underwent minor changes. The cation intermixing (Li^{+}/Ni^{2+}) also increased from 4.3 % to 6.8 % in the case of NCM83@Si-0, accompanied by a significant decrease in $I_{(003)}/I_{(104)}$ ratio (from 1.51 to 1.38) due to Ni^{2+} occupying lithium-site vacancies [12]. In contrast, NCM83@Si-10 experienced much less cation intermixing, with the $I_{(003)}/I_{(104)}$ ratio remaining at 1.50 after 28 days of exposure, corroborating that the coating indeed mitigates structural degradation upon air exposure.

Overall, the Si-based coating significantly improved the air/moisture stability of NCM83 by strongly suppressing the formation of surface impurities and reducing lithium migration, thus preserving the material's structural integrity.

3.3. Electrochemical stability before and after air exposure

The electrochemical performance of the as-synthesized cathodes was evaluated in CR2032-type half cells with lithium metal as the anode. **Figure S8** presents the initial charge/discharge curves for the pristine materials at a rate of 0.1C (with 1C = 180 mA g^{-1}). All samples showed similar voltage profiles, indicating no additional electrochemical reactions due to the silicon modification. The initial specific discharge capacities of NCM83@Si-0, NCM83@Si-5, NCM83@Si-10, and NCM83@Si-15 were 205, 204, 204, and 202 mAh g^{-1}, respectively, with corresponding Coulomb efficiencies of 82.3 %, 83.5 %, 85.2 %, and 84.7 %. These results indicate that the Li_xSiO_y coating enhances the electrochemical reversibility, although excessive modification leads to some capacity loss. Cyclic voltammetry (CV) measurements performed in the same potential window of 2.8–4.3 V vs. Li^{+}/Li (0.1 mV s^{-1}) revealed three distinct peaks for NCM83@Si-0 and NCM83@Si-10, corresponding to the phase transitions from H1 to M, M to H2, and H2 to H3 (see **Figure S8**) [29]. The redox peak potential difference (ΔE) for NCM83@Si-10 (47.2 mV) was found to be smaller than that for NCM83@Si-0 (67.2 mV), suggesting reduced polarization and increased stability in the coated cathode [30]. Long-term cycling performance testing further demonstrated that the modified NCM83 exhibits significantly improved capacity retention, with NCM83@Si-10 retaining 94.7 % of its capacity after 100 cycles at 1C, compared to only 74.5 % for NCM83@Si-0 (see Fig. 4**a**). The charge/discharge curves in Fig. 4**b** and **c** indicate significant voltage fluctuations for NCM83@Si-0 due to polarization, while NCM83@Si-10 revealed much more stable profiles, as supported by the differential capacity curves shown in **Figure S9**. The enhanced stability of NCM83@Si-10 is attributed to its higher structural robustness during battery operation.

Increasing the operating voltage window of LIBs is essential for meeting the growing demand for high-energy-density storage systems. However, high cut-off potentials (states of charge) increase the formation of Ni^{4+} [31], which can destabilize the layered structure through transition-metal dissolution and surface degradation [32]. Testing the NCM83@Si-0 and NCM83@Si-10 cathodes in a potential range between 2.8 and 4.5 V vs. Li^{+}/Li (see Fig. 4**d**) showed that NCM83@Si-10 is capable of maintaining 87.9 % of its capacity after 100 cycles at 1C, while NCM83@Si-0 exhibited only 70.2 % retention, demonstrating that the surface coating indeed helps reduce electrolyte interaction with

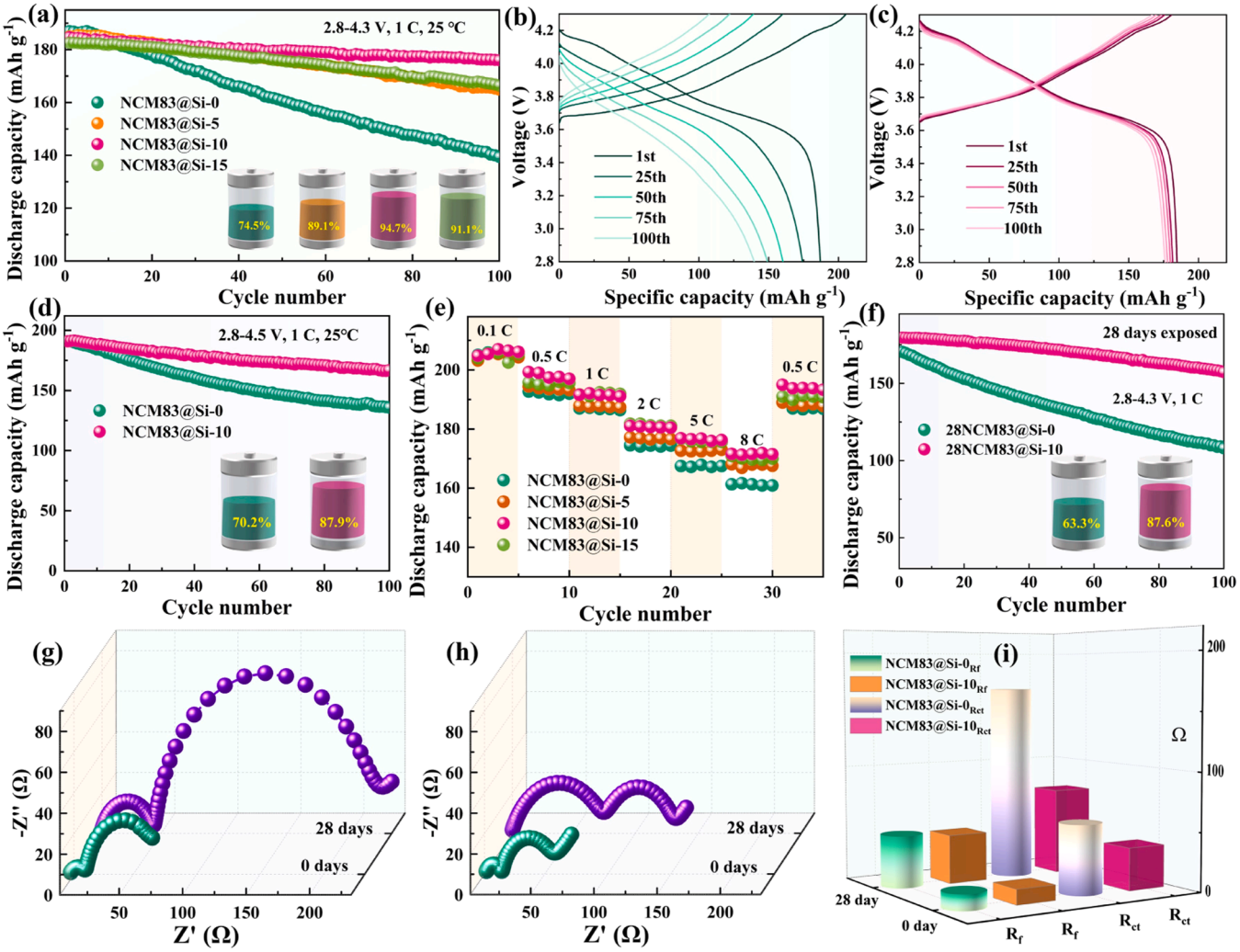

Fig. 4. (a) Cycling performance of the pristine coated and uncoated cathodes at 1C rate in the potential window of 2.8–4.3 V vs. Li^+/Li and corresponding charge/discharge curves of (b) NCM83@Si-0 and (c) NCM83@Si-10. (d) Cycling performance of NCM83@Si-0 and NCM83@Si-10 at 1C rate in the potential window of 2.8–4.5 V vs. Li^+/Li. (e) Rate capability of the pristine coated and uncoated cathodes. (f) Cycling performance of 28NCM83@Si-0 and 28NCM83@Si-10 (1C rate, 2.8–4.3 V vs. Li^+/Li). Nyquist plots of the electrochemical impedance for (g) NCM83@Si-0 and (h) NCM83@Si-10 before and after air exposure and (i) results from curve fitting.

reactive Ni^{4+} (see also voltage profiles in **Figure S10**). The rate performance of the as-prepared cathodes was also examined, as shown in Fig. 4**e**. At 0.1C, all samples delivered similar capacities. However, the Li_xSiO_y-modified cathodes clearly outperformed the uncoated NCM83@Si-0 upon increasing the current density. Notably, NCM83@Si-10 retained a specific discharge capacity of 172 mAh g^{-1} at 8C, compared to 161 mAh g^{-1} for NCM83@Si-0. CV analysis further confirmed improved kinetics for NCM83@Si-10 (see **Figure S11**), with Li-ion diffusion coefficients of 2.04 × 10^{-14} and 1.27 × 10^{-14} cm^2 s^{-1} between 2.7 and 4.3 V, significantly higher than those of NCM83@Si-0 (6.97 × 10^{-15} and 4.98 × 10^{-15} cm^2 s^{-1}). This is due to the Li_xSiO_y coating being present, reducing interfacial impedance and promoting homogeneous ion flux across the electrode|electrolyte interface.

The chemical stability of NCM83@Si-0 and NCM83@Si-10 toward H_2O and CO_2 was investigated by assessing their cycling stability after 28 days of air exposure (see Fig. 4**f**). The NCM83@Si-0 cathode experienced a sharp decline in initial specific capacity from 187 to 170 mAh g^{-1} (2.8–4.3 V vs. Li^+/Li), leading to inferior capacity retention of 63.3 % (108 mAh g^{-1}) after 100 cycles at 1C. This degradation is attributed to the loss of active lithium and surface phase transformations that impede ion diffusion. In contrast, the NCM83@Si-10 cathode maintained a reversible specific capacity of 157 mAh g^{-1} (87.6 % capacity retention) after 100 cycles, indicating that the protective coating effectively prevents surface reactions with moisture, thereby enhancing both the storage stability under ambient conditions and the cycling performance.

Electrochemical impedance spectroscopy (EIS) measurements were also performed to examine the interfacial kinetics before and after air exposure (see Fig. 4**g** and **h**). The impedance spectra (Nyquist plots) exhibited two depressed semicircles and a Warburg-like capacitive tail, with the high- and mid-frequency semicircles corresponding to the cathode electrolyte interphase (CEI) resistance and charge-transfer resistance at the electrode|electrolyte interface, respectively [33,34]. The low-frequency capacitive tail represents ion diffusion within the material [35]. Fitting the EIS data (see Fig. 4**i** and **Figure S12**) revealed no significant differences between the cathodes prior to air exposure. However, after 28 days, the charge-transfer resistance (R_{ct}) of NCM83@Si-0 increased to 167 Ω, indicating impaired interfacial kinetics due to surface degradation, whereas NCM83@Si-10 revealed a much lower R_{ct} of 75 Ω. This provides further evidence that the Li_xSiO_y coating improves the surface integrity by increasing chemical stability.

3.4. *Enhanced structural stability under ambient air conditions*

The degradation mechanism observed suggests that Ni-rich cathode

particles readily adsorb H_2O and CO_2 from the atmosphere, resulting in residual lithium formation and Ni^{3+} reduction after air exposure. X-ray absorption near edge structure (XANES) spectroscopy measurements were conducted on the NCM83@Si-0 and NCM83@Si-10 after different air exposure durations. In the case of uncoated NCM83, the Ni K-edge shifted significantly from 8352.1 eV (after 14 days) to 8350.1 eV (after 28 days), indicating increased Ni^{2+} concentration due to surface degradation (see Fig. 5**a**). In contrast, NCM83@Si-10 exhibited only a minor shift, with the Ni oxidation state(s) remaining rather stable (see Fig. 5**b** and **c**). While increasing the Ni content increases the specific capacity in layered oxide cathodes, it also facilitates irreversible reduction of Ni^{3+} to Ni^{2+} upon air exposure, causing cation mixing and transformation of the layered structure into redox-inactive rock-salt phase.

Extended X-ray absorption fine structure (EXAFS) analysis was also performed to study the evolution of the local chemical environment of Ni during air exposure. Fig. 5**d** and **e** shows two major peaks located at 1–2 Å and 2–3 Å, corresponding to the nearest oxygen (Ni–O bonds) and transition metals (Ni–TM bonds) around the Ni atoms. After 28 days, the Ni–O and Ni–TM bond distances in NCM83@Si-0 increased, indicating Ni^{2+} accumulation from surface deterioration. In contrast, NCM83@Si-10 maintained consistent bond lengths, confirming enhanced stability against moisture. (2D contour) Fourier-transformed Ni K-edge EXAFS analysis further demonstrated stable bond lengths and intensities in NCM83@Si-10, emphasizing the protective role of the Li_xSiO_y coating (see Fig. 5**f** and **Figures S13** and **S14**). By contrast, the bond lengths and intensities in NCM83@Si-0 showed significant attenuation after 28 days of air exposure, which can be attributed to the

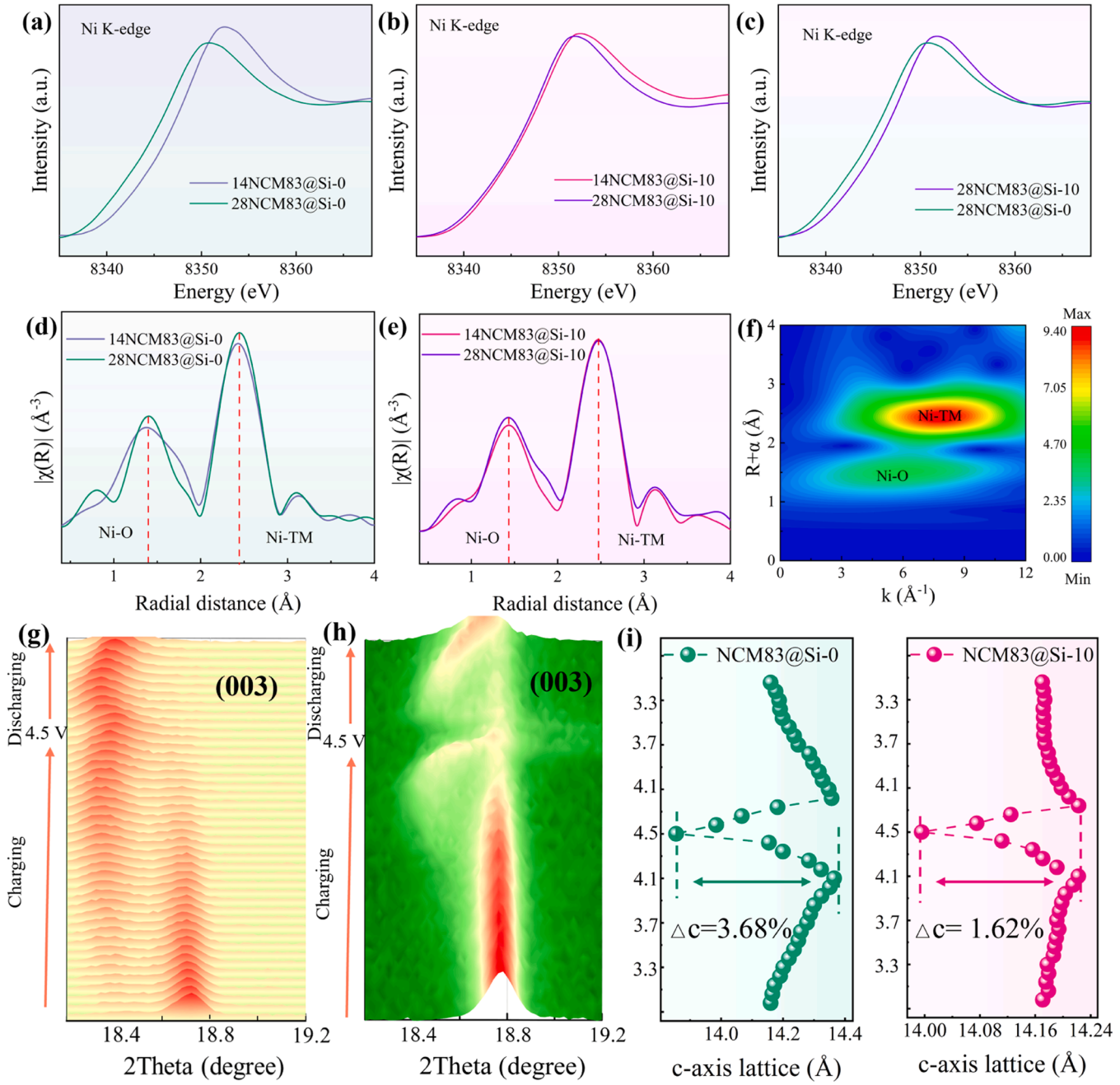

Fig. 5. (a–c) *Ex situ* Ni K-edge XANES spectra of NCM83@Si-0 and NCM83@Si-10 after 14 and 28 days of air exposure and (d, e) corresponding Ni K-edge EXAFS spectra. (f) 2D FT Ni K-edge EXAFS spectrum of 14NCM83@Si-10. *In situ* XRD of the (003) reflection during the first cycle between 2.8 and 4.5 V vs. Li^+/Li for (g) 28NCM83@Si-0 and (h) 28NCM83@Si-10 and (i) corresponding unit-cell parameter changes along the *c*-axis.

formation of lithium vacancies caused by ion diffusion from the bulk to the surface.

To gain insights into the effect that the surface modification strategy after 28 days of air exposure has on the phase transitions occurring during cycling, in situ XRD was employed to monitor the structural evolution of both NCM83@Si-0 and NCM83@Si-10 upon (de)lithiation. Both cathodes showed a similar shift in (003) reflection, representing changes in *c*-axis parameter (see Fig. 5**g** and **h**) [36]. The initial shift to lower angles during charge corresponds to the H1-M-H2 transitions and *c*-axis expansion [31]. Further delithiation resulted in a pronounced shift to higher angles, indicating lattice contraction and H3 phase formation due to increased Ni^{4+}–O^{2-} bond covalence [37]. The latter typically induces mechanical stress and leads to particle fracture. Notably, 28NCM83@Si-10 exhibited a smaller shift during the H2-H3 transition compared to 28NCM83@Si-0 (by 0.296° vs. 0.780° at 4.3 V), thus reducing stress accumulation. Additionally, the *c*-axis shrinkage (see Fig. 5**i**) was significantly lower for NCM83@Si-10 (1.6 %) compared to NCM83@Si-0 (3.7 %), indicating that the Li_xSiO_y coating helps mitigate the internal strain associated with the detrimental H2-H3 phase transition.

Post mortem characterizations were conducted on the NCM83@Si-0 and NCM83@Si-10 cathodes that underwent 28 days of air exposure to examine the cumulative structural degradation after extended cycling (100 cycles). XRD patterns collected before and after cycling (see Fig. 6**a**) revealed the characteristic reflections of the layered structure. For 28NCM83@Si-0, a notable reduction in peak intensity indicated mechanical fatigue. Moreover, as expected (see Fig. 6**b**), a smaller shift in (003) reflection was observed for 28NCM83@Si-10 (by 0.14°) compared to 28NCM83@Si-0 (by 0.60°). Likewise, the transition-metal leaching from the 28NCM83@Si-10 cathode was significantly lower, as can be seen in Fig. 6**c**, indicating that the protective coating helps prevent electrolyte-induced surface corrosion.

Morphological changes to the materials were examined via surface and cross-sectional SEM. The analysis revealed severe intergranular cracking of the 28NCM83@Si-0 particles (see Fig. 6**d** and **e**), caused by the continuous anisotropic lattice-parameter changes during electrochemical cycling. These cracks propagated to the surface (mainly along the grain boundaries), compromising mechanical integrity. In contrast, the 28NCM83@Si-10 particles showed fewer microcracks (see Fig. 6**g** and **h**), confirming enhanced resistance toward mechanical stress. The

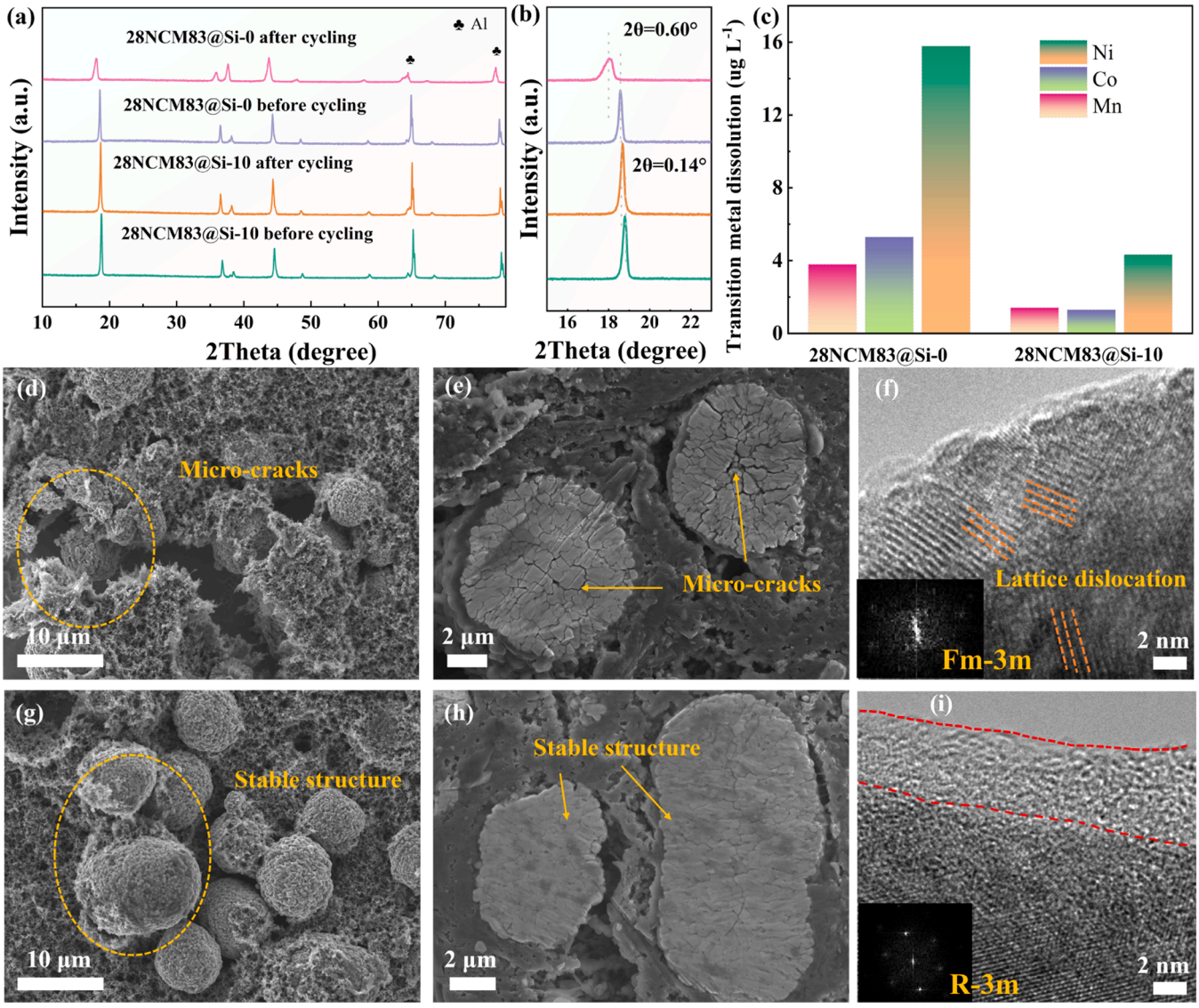

Fig. 6. (a) XRD patterns and (b) zoomed-in view of the (003) reflection for 28NCM83@Si-0 and 28NCM83@Si-10 before and after 100 cycles. (c) TM leaching upon cycling. (d–i) Top-view and cross-sectional SEM images as well as HRTEM images collected from the (d–f) 28NCM83@Si-0 and (g–i) 28NCM83@Si-10 cathodes after cycling.

formation of microcracks in 28NCM83@Si-0 provided channels for electrolyte penetration, leading to parasitic side reactions and transition-metal dissolution, as confirmed by XPS analysis. Unlike 28NCM83@Si-0, the P 2p spectrum collected from the cycled 28NCM83@Si-10 cathode revealed minor $Li_xPO_yF_z/Li_xPF_y$ formation (see **Figure S15**), thus suggesting fewer side reactions at the electrode|electrolyte interface [38].

High-resolution TEM (HRTEM) further demonstrated that the cycled 28NCM83@Si-10 maintained its layered structure ($R-3m$ space group; see Fig. 6**f**). In contrast, the surface of the 28NCM83@Si-0 particles underwent severe degradation (see Fig. 6**i**), transforming into a NiO-like rock-salt phase ($Fm-3m$ space group) and increasing the energy barrier for lithium (de)intercalation, thus ultimately compromising the cyclability.

To better understand the chemical degradation mechanisms at the electrode|air interface, theoretical calculations of the adsorption free energies of H_2O and CO_2, coupled with *ex situ* XPS analysis, were performed. The most stable planes, (111) for NCM83 and (001) for the Si-based coating, were selected for the calculations (see Fig. 7**a**–**c**). The results indicated that the formation of residual lithium species on NCM83@Si-0 is thermodynamically favorable ($\Delta G = -1.416$ eV). In contrast, the NCM83@Si-10 exhibited a positive ΔG value (0.154 eV),

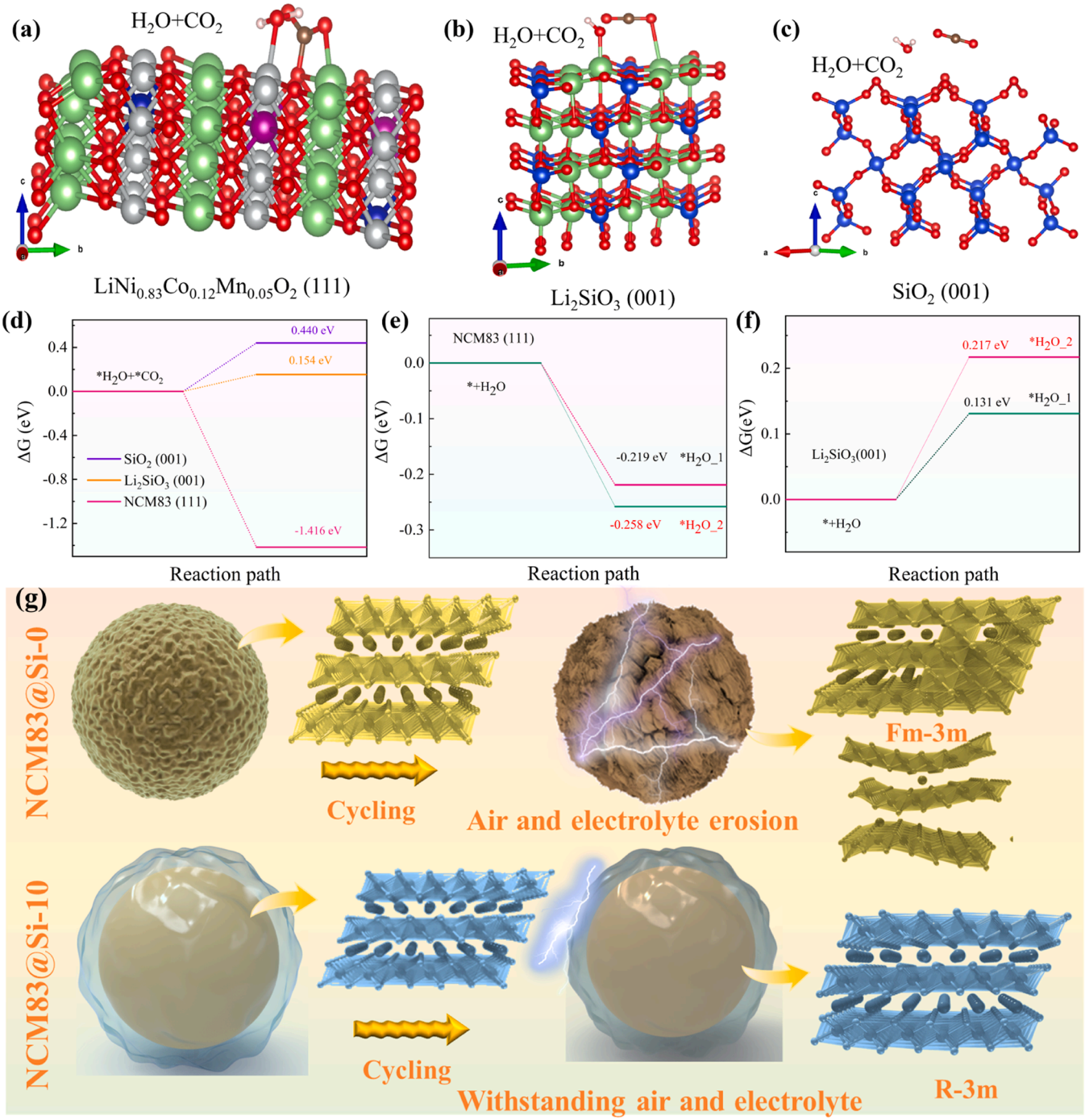

Fig. 7. (a–d) Theoretical calculations of adsorption free energies for H_2O and CO_2 on (a) NCM83 (111), (b) Li_2SiO_3 (001), and (c) SiO_2 (001) surfaces. Adsorption free energies of a single H_2O molecule on (e) NCM83 (111) and (f) Li_2SiO_3 (001) surfaces considering two configurations. (g) Schematics of the working principle of pristine and coated NCM83.

demonstrating enhanced air stability due to the protective coating, which increases the formation energy (see Fig. 7**d**). The adsorption free energy of H_2O is a key factor in surface reactions upon air exposure, as its adsorption within the inner Helmholtz layer is essential for subsequent reactions [39]. Stronger adsorption correlates with a higher propensity for surface reactions following air exposure. As demonstrated in **Figures S16–S18**, two adsorption configurations for a single H_2O molecule are considered when evaluating the free energy. The adsorption free energy for the H_2O/NCM83@Si-0(111) interface is −0.258 and −0.219 eV (see Fig. 7**e**), indicating that the cathode material can be wetted well by H_2O. In comparison, the Si-based (001) surface showed much higher adsorption free energies of 0.217 and 0.131 eV, manifesting reduced wettability and moisture uptake (see Fig. 7**f**). It should be noted that SiO_2 exhibited even higher adsorption free energies (0.408 and 0.378 eV), but the inferior ionic conductivity limits its application (see **Figure S19**). Overall, the theoretical calculations confirm that the presence of a uniform Li_2SiO_3 surface coating inhibits physical contact between the NCM83 and H_2O, thus reducing air/moisture-induced side reactions and preserving electrochemical performance.

Both nickel migration and cation mixing were also assessed, as these processes induce irreversible phase transitions. For NCM83@Si-0, extended air exposure led to the formation of Li_2CO_3 and LiOH on the surface, driven by Ni^{3+} reduction (see **Figures S20** and **S21**) [10,15,40]. The reduction of Ni^{3+} to Ni^{2+} occurs due to the better stability of Ni^{2+} under ambient conditions. Ni^{3+}, with its low-spin $t2g^6eg^1$ electronic configuration, undergoes Jahn-Teller distortion, leading to disproportionation into Ni^{2+} and Ni^{4+}. Simultaneously, the reduction of Ni^{3+} causes oxidation of O^{2-} (lattice oxygen) to O^- (active oxygen), thereby weakening the Ni−O bonds. This active oxygen then undergoes disproportionation into O^{2-} and O, which in turn reacts with both the CO_2 and H_2O present in the air to form CO_3^{2-} and OH^-, eventually resulting in the formation of surface contaminants, such as LiOH and Li_2CO_3. In contrast, the NCM83@Si-10 cathode maintains stable Ni^{2+}/Ni^{3+} ratio (see **Figures S21**), preventing unwanted side reactions by limiting nickel reduction at the electrode|air interface.

Based on the aforementioned observations, Fig. 7**g** illustrates the working principle of the surface modification strategy. Overall, the parasitic surface reactions discussed above impair the electrochemical activity by hindering lithium diffusion and increasing the energy barrier for (de)lithiation. In addition, particle fracture caused by anisotropic volume variations, especially during the detrimental H2-H3 phase transition at high states of charge, accelerates capacity degradation. However, the Si-based coating is capable of mitigating these issues by reducing surface wettability, increasing chemical stability, and improving mechanical robustness of the cathode.

4. Conclusions

The inherent chemical instability of NCM83 under ambient conditions can be mitigated by grafting a Li_xSiO_y coating onto the secondary particle surface. Structural characterization and DFT calculations demonstrate that the protective coating strongly reduces the hydrophilicity, suppresses the formation of residual lithium species, and prevents undesired phase transformations upon air exposure. It also improves the mechanical resilience, alleviating isotropic strain-induced particle fracture and delamination cracking during prolonged battery operation. With 28 days of air exposure, the coated cathode is still capable of delivering a high specific capacity of 157 mAh g^{-1} after 100 cycles at 1C (87.6 % capacity retention), clearly outperforming the uncoated counterpart (108 mAh g^{-1}, 63.3 % capacity retention). Taken together, this study provides a promising strategy for advancing Ni-rich cathodes, offering insights into addressing atmospheric stability issues of air-sensitive battery materials.

CRediT authorship contribution statement

Zhouliang Tan: Writing – original draft, Validation, Investigation, Data curation. **Feng Xu:** Writing – review & editing, Investigation, Data curation. **Ruizhuo Zhang:** Validation, Investigation, Data curation. **Yudai Huang:** Writing – review & editing, Supervision. **Xia Liu:** Writing – review & editing, Investigation. **Shupeng Yang:** Investigation, Data curation. **Yizhong Guo:** Investigation. **Qingcui Liu:** Writing – review & editing. **Tianlong Wu:** Writing – original draft, Data curation. **Yingde Huang:** Writing – review & editing, Supervision, Conceptualization. **Torsten Brezesinski:** Writing – review & editing, Validation, Data curation. **Yu Tang:** Writing – review & editing, Supervision. **Wengao Zhao:** Writing – review & editing, Validation, Supervision, Data curation.

Declaration of competing interest

The authors declare that they have no known competing financial interests or personal relationships that could have appeared to influence the work reported in this paper.

Acknowledgement

This work was financially supported by the National Natural Science Foundation of China (52162036, 22378342, 22221001, and 22131007) and the 111 project (B20027), the Key Project of Nature Science Foundation of Xinjiang Province (2021D01D08), the Major Projects of Xinjiang Province (2022A01005–4 and 2021A01001–1), the Key Research and Development Project of Xinjiang Province (2023B01025–1), and the Xinjiang Tianchi Yingcai Project.

Supplementary materials

Supplementary material associated with this article can be found, in the online version, at doi:10.1016/j.ensm.2025.104169.

Data availability

Data will be made available on request.

References

[1] M. Li, J. Lu, Z. Chen, K. Amine, 30 Years of lithium-ion batteries, Adv. Mater. 30 (2018) 1800561.
[2] B.E. Murdock, K.E. Toghill, N. Tapia-Ruiz, A perspective on the sustainability of cathode materials used in lithium-ion batteries, Adv. Energy Mater. 11 (2021) 2102028.
[3] A. Chakraborty, S. Kunnikuruvan, S. Kumar, B. Markovsky, D. Aurbach, M. Dixit, D.T. Major, Layered cathode materials for lithium-ion batteries: review of computational studies on $LiNi_{1-x-y}Co_xMn_yO_2$ and $LiNi_{1-x-y}Co_xAl_yO_2$, Chem. Mater. 32 (2020) 915–952.
[4] Y. Lyu, X. Wu, K. Wang, Z. Feng, T. Cheng, Y. Liu, M. Wang, R. Chen, L. Xu, J. Zhou, Y. Lu, B. Guo, An overview on the advances of $LiCoO_2$ cathodes for lithium-ion batteries, Adv. Energy Mater. 11 (2021) 2000982.
[5] G. Yan, J. Wei, E. Apodaca, S. Choi, P.J. Eng, J.E. Stubbs, Y. Han, S. Zou, M.K. Bera, R. Wu, E. Karapetrova, H. Zhou, W. Chen, C. Liu, Identifying critical features of iron phosphate particle for lithium preference, Nat. Commun. 15 (2024) 4859.
[6] D. Tang, Y. Sun, Z. Yang, L. Ben, L. Gu, X. Huang, Surface structure evolution of $LiMn_2O_4$ cathode material upon charge/discharge, Chem. Mater. 26 (2014) 3535–3543.
[7] J.U. Choi, N. Voronina, Y.-K. Sun, S.-T. Myung, Recent progress and perspective of advanced high-energy Co-less Ni-rich cathodes for Li-ion batteries: yesterday, today, and tomorrow, Adv. Energy Mater. 10 (2020) 2002027.
[8] U.-H. Kim, G.-T. Park, B.-K. Son, G.W. Nam, J. Liu, L.-Y. Kuo, P. Kaghazchi, C. S. Yoon, Y.-K. Sun, Heuristic solution for achieving long-term cycle stability for Ni-rich layered cathodes at full depth of discharge, Nat. Energy 5 (2020) 860–869.
[9] J. Yang, X. Liang, H.-H. Ryu, C.S. Yoon, Y.-K. Sun, Ni-rich layered cathodes for lithium-ion batteries: from challenges to the future, Energy Storage Mater 63 (2023) 102969.
[10] W. Zhang, C. Yuan, J. Zhu, T. Jin, C. Shen, K. Xie, Air instability of Ni-Rich layered oxides–A roadblock to large scale application, Adv. Energy Mater. 13 (2023) 2202993.

[11] L. Zeng, K. Shi, B. Qiu, H. Liang, J. Li, W. Zhao, S. Li, W. Zhang, Z. Liu, Q. Liu, Hydrophobic surface coating against chemical environmental instability for Ni-rich layered oxide cathode materials, Chem. Eng. J. 437 (2022) 135276.
[12] C. Lv, Z. Li, X. Ren, K. Li, J. Ma, X. Duan, Revealing the degradation mechanism of Ni-rich cathode materials after ambient storage and related regeneration method, J. Mater. Chem. A 9 (2021) 3995–4006.
[13] Y. Xia, A. Chen, K. Wang, Q. Mao, H. Huang, J. Zhang, X. He, Y. Gan, Z. Xiao, W. Zhang, Industrial modification comparison of Ni-Rich cathode materials towards enhanced surface chemical stability against ambient air for advanced lithium-ion batteries, Chem. Eng. J. 450 (2022) 138382.
[14] H. Li, L. Wang, Y. Song, Y. Wu, H. Zhang, A. Du, X. He, Understanding the insight mechanism of chemical-mechanical degradation of layered Co-free Ni-rich cathode materials: a review, Small 19 (2023) 2302208.
[15] S.S. Zhang, Problems and their origins of Ni-rich layered oxide cathode materials, Energy Storage Mater. 24 (2020) 247–254.
[16] S. Yin, W. Deng, J. Chen, X. Gao, G. Zou, H. Hou, X. Ji, Fundamental and solutions of microcrack in Ni-rich layered oxide cathode materials of lithium-ion batteries, Nano Energy 83 (2021) 105854.
[17] M. Jiang, D.L. Danilov, R.-A. Eichel, P.H.L. Notten, A review of degradation mechanisms and recent achievements for Ni-rich cathode-based Li-ion batteries, Adv. Energy Mater. 11 (2021) 2103005.
[18] W. Lee, S. Lee, E. Lee, M. Choi, R. Thangavel, Y. Lee, W.-S. Yoon, Destabilization of the surface structure of Ni-rich layered materials by water-washing process, Energy Storage Mater. 44 (2022) 441–451.
[19] J. Wang, Z. Zhang, W. He, Z. Wang, S. Weng, Q. Li, X. Wang, S. Barg, L. Chen, H. Li, F. Wu, Fast charge storage kinetics by surface engineering for Ni-rich layered oxide cathodes, J. Mater. Chem. A 11 (2023) 10239–10253.
[20] Y. Kato, A. Nagahara, N. Gerile, S. Fujinaka, N. Hamamoto, H. Nishimura, H. Nakai, Investigation of water-washing effect on electrochemical properties of Ni-rich NCA cathode material for lithium-ion batteries, J. Electrochem. Soc. 169 (2022) 060543.
[21] Y. Su, L. Li, G. Chen, L. Chen, N. Li, Y. Lu, L. Bao, S. Chen, F. Wu, Strategies of removing residual lithium compounds on the surface of Ni-rich cathode materials†, Chin. J. Chem. 39 (2021) 189–198.
[22] Y. Wu, H. Wu, J. Deng, Z. Han, X. Xiao, L. Wang, Z. Chen, Y. Deng, X. He, Insight of synthesis of single crystal Ni-rich $LiNi_{1-x-y}Co_xMn_yO_2$ cathodes, Adv. Energy Mater. 14 (2024) 2303758.
[23] Y. Huang, P.-Y. Li, H.-X. Wei, Y.-H. Luo, L.-B. Tang, H.-Z. Chen, X.-h. Zhang, J.-c. Zheng, Suppress moisture sensitivity of Ni-rich cathode materials by bioinspired self-assembly hydrophobic layer, Chem. Eng. J. 477 (2023) 146850.
[24] H.-H. Ryu, H.-W. Lim, S.G. Lee, Y.-K. Sun, Near-surface reconstruction in Ni-rich layered cathodes for high-performance lithium-ion batteries, Nat. Energy 9 (2024) 47–56.
[25] Y. Kim, H. Park, J.H. Warner, A. Manthiram, Unraveling the intricacies of residual lithium in high-Ni cathodes for lithium-ion batteries, ACS Energy Lett. 6 (2021) 941–948.
[26] Y.-H. Du, H. Sheng, X.-H. Meng, X.-D. Zhang, Y.-G. Zou, J.-Y. Liang, M. Fan, F. Wang, J. Tang, F.-F. Cao, J.-L. Shi, X.-F. Cao, Y.-G. Guo, Chemically converting residual lithium to a composite coating layer to enhance the rate capability and stability of single-crystalline Ni-rich cathodes, Nano Energy 94 (2022) 106901.
[27] Z. Tan, Y. Li, C. Lei, Y. Li, X. Xi, S. Jiang, F. Wu, Z. He, In situ constructing ultrastable mechanical integrity of single-crystalline $LiNi_{0.9}Co_{0.05}Mn_{0.05}O_2$ cathode by interior and exterior decoration strategy, Small 20 (2024) 2305618.
[28] C. Zhang, X. Wu, C. Chen, F. Xing, C. Liang, M. Song, L. Zhang, W. Wei, Origin of environmentally structural susceptibility of nickel-based layered oxide cathodes, Acta Mater. 261 (2023) 119392.
[29] Z. Tan, X. Chen, Y. Li, X. Xi, S. Hao, X. Li, X. Shen, Z. He, W. Zhao, Y. Yang, Enabling superior cycling stability of $LiNi_{0.9}Co_{0.05}Mn_{0.05}O_2$ with controllable internal strain, Adv. Funct. Mater. 33 (2023) 2215123.
[30] X. Zhang, J. Lin, E. Fan, Q. Huang, S. Ma, R. Chen, F. Wu, L. Li, Insight into the capacity degradation and structural evolution of single-crystal Ni-rich cathodes, J. Energy Chem. 95 (2024) 68–76.
[31] S.H. Song, M. Cho, I. Park, J.-G. Yoo, K.-T. Ko, J. Hong, J. Kim, S.-K. Jung, M. Avdeev, S. Ji, S. Lee, J. Bang, H. Kim, High-voltage-driven surface structuring and electrochemical stabilization of Ni-rich layered cathode materials for Li rechargeable batteries, Adv. Energy Mater. 10 (2020) 2000521.
[32] X. Fan, X. Ou, W. Zhao, Y. Liu, B. Zhang, J. Zhang, L. Zou, L. Seidl, Y. Li, G. Hu, C. Battaglia, Y. Yang, In situ inorganic conductive network formation in high-voltage single-crystal Ni-rich cathodes, Nat. Commun. 12 (2021) 5320.
[33] X. Li, H. Guan, Z. Ma, M. Liang, D. Song, H. Zhang, X. Shi, C. Li, L. Jiao, L. Zhang, In/ex-situ Raman spectra combined with EIS for observing interface reactions between Ni-rich layered oxide cathode and sulfide electrolyte, J. Energy Chem. 48 (2020) 195–202.
[34] Y.-S. Kang, S.Y. Park, K. Ito, Y. Kubo, Y. Shin, D.Y. Kim, D.-H. Seo, S. Kim, J.-H. Park, S.-G. Doo, M. Koh, J.A. Seo, K. Park, Revealing the structural degradation mechanism of the Ni-rich cathode surface: how thick is the surface? J. Power Sources 490 (2021) 229542.
[35] Z. Tan, Y. Li, X. Xi, S. Jiang, X. Li, X. Shen, P. Zhang, Z. He, J. Zheng, A novelty strategy induced pinning effect and defect structure in Ni-rich layered cathodes towards boosting its electrochemical performance, J. Energy Chem. 72 (2022) 570–580.
[36] B. Wu, Z. Lin, G. Zhang, D. Zhang, W. Zhang, G. Li, Y. Che, L. Chen, H. Wang, W. Li, M. Chen, G. Cao, In situ mitigating cation mixing of Ni-rich cathode at high voltage via Li_2MnO_3 injection, Energy Storage Mater. 53 (2022) 212–221.
[37] Z. Dai, H. Zhao, W. Chen, Q. Zhang, X. Song, G. He, Y. Zhao, X. Lu, Y. Bai, In situ construction of gradient oxygen release buffer and interface cation self-accelerator stabilizing high-voltage Ni-rich cathode, Adv. Funct. Mater. 32 (2022) 2206428.
[38] B. Namkoong, N.-Y. Park, G.-T. Park, J.-Y. Shin, T. Beierling, C.S. Yoon, Y.-K. Sun, High-energy Ni-rich cathode materials for long-range and long-life electric vehicles, Adv. Energy Mater. 12 (2022) 2200615.
[39] J. Hu, W. Ren, X. Chen, Y. Li, W. Huang, K. Yang, L. Yang, Y. Lin, J. Zheng, F. Pan, The role of anions on the Helmholtz Plane for the solid-liquid interface in aqueous rechargeable lithium batteries, Nano Energy 74 (2020) 104864.
[40] W. Wei, Z. Wang, L. Yao, H. Jiang, C. Li, Stabilizing lattice oxygen and interface chemistry of Ni-rich and Co-poor cathodes for high-energy lithium-ion batteries, J. Mater. Chem. A 11 (2023) 2979–2984.